Article

Cholesterol Modulates CFTR Confinement in the Plasma Membrane of Primary Epithelial Cells

Asmahan Abu-Arish,[1] Elvis Pandzic,[2] Julie Goepp,[3] Elizabeth Matthes,[3] John W. Hanrahan,[3] and Paul W. Wiseman[4,*]

[1]Physics and Physiology, [2]Physics, [3]Physiology, and [4]Chemistry & Physics, McGill University, Montreal, Quebec, Canada

ABSTRACT   The cystic fibrosis transmembrane conductance regulator (CFTR) is a plasma-membrane anion channel that, when mutated, causes the disease cystic fibrosis. Although CFTR has been detected in a detergent-resistant membrane fraction prepared from airway epithelial cells, suggesting that it may partition into cholesterol-rich membrane microdomains (lipid rafts), its compartmentalization has not been demonstrated in intact cells and the influence of microdomains on CFTR lateral mobility is unknown. We used live-cell imaging, spatial image correlation spectroscopy, and k-space image correlation spectroscopy to examine the aggregation state of CFTR and its dynamics both within and outside microdomains in the plasma membrane of primary human bronchial epithelial cells. These studies were also performed during treatments that augment or deplete membrane cholesterol. We found two populations of CFTR molecules that were distinguishable based on their dynamics at the cell surface. One population showed confinement and had slow dynamics that were highly cholesterol dependent. The other, more abundant population was less confined and diffused more rapidly. Treatments that deplete the membrane of cholesterol caused the confined fraction and average number of CFTR molecules per cluster to decrease. Elevating cholesterol had the opposite effect, increasing channel aggregation and the fraction of channels displaying confinement, consistent with CFTR recruitment into cholesterol-rich microdomains with dimensions below the optical resolution limit. Viral infection caused the nanoscale microdomains to fuse into large platforms and reduced CFTR mobility. To our knowledge, these results provide the first biophysical evidence for multiple CFTR populations and have implications for regulation of their surface expression and channel function.

INTRODUCTION

The cystic fibrosis transmembrane conductance regulator (CFTR) is a tightly regulated anion channel expressed at the apical surface of epithelial cells (1,2). Anion flux through the CFTR drives transepithelial fluid secretion and is required for efficient mucociliary clearance of inhaled bacteria and other particles from the lung (reviewed by Frizzell and Hanrahan (3)). Mutations in the *cftr* gene cause cystic fibrosis (CF), an autosomal recessive disease characterized by diminished salt and fluid secretion, accumulation of viscid mucus, and recurring cycles of airway infection by *Staphylococcus aureus*, *Pseudomonas aeruginosa*, and other pathogens. Most morbidity and mortality in CF results from chronic inflammation of the airways and the resulting gradual decline in lung function.

The CFTR associates with other proteins in a macromolecular complex, and its channel activity and surface expression are regulated by local signaling and recycling through endosomal compartments, respectively. These processes are expected to depend on the compartmentalization and lateral mobility of CFTR and its interactome, although CFTR dynamics at the cell surface are not well understood. Most studies have focused on protein-protein interactions,

but lipids may also play a role in compartmentalizing CFTR. About half of the CFTR in Calu-3, an airway epithelial cell line, is found in a detergent-resistant membrane (DRM) fraction hypothesized to include lipid rafts (4). Rafts are hypothesized nanoscale microdomains in the plasma membrane that are enriched in cholesterol and glycosphingolipids (5,6) and are thought to cluster receptors and intracellular signaling molecules including G protein coupled receptors (7), tumor necrosis factor receptor (8), and kinases, notably Src (8,9) and protein kinase C (10,11).

Activation of the tumor necrosis factor receptor and inhibition of Src kinase increases the association of these signaling molecules with lipid raft components and is accompanied by recruitment of the CFTR to the DRM fraction (8), suggesting that the CFTR may partition into microdomains during inflammation. This partitioning may be due to lipid interactions with CFTR itself or with the scaffold protein NHERF1, which links the CFTR to the actin cytoskeleton (12) and also binds to cholesterol at the plasma membrane (13). Colocalization of fluorescently labeled CFTR with the lipid raft markers cholera toxin B or caveolin-1 has also been observed during infection by *Pseudomonas aeruginosa* (14–16), and the CFTR has been proposed to bind and internalize bacteria to help clear them from the lumen and to initiate lipid-raft-dependent epithelial cytokine and chemokine release (8,14–17). The

presence of a CFTR population in the DRM fraction implies heterogeneity among CFTR molecules. Only one homogeneous population of CFTR channels was detected based on single-particle tracking (18), so it remains uncertain whether some CFTR channels are present in lipid rafts under resting conditions and whether this distribution influences their lateral mobility.

In this work, we quantified the distribution of CFTR in primary human bronchial epithelial cells using spatial image correlation spectroscopy (ICS (19)) and studied CFTR dynamics using a modified version of k-space ICS (kICS (20,21)). To identify the CFTR population that is in cholesterol-rich membrane microdomains, transport and partitioning dynamics were compared under control conditions and after treatment with cholesterol oxidase or cholesterol esterase to deplete or augment cholesterol, respectively. kICS analysis revealed two dynamically distinct populations of CFTR on the plasma membrane, one of which had large (relative to the focal-spot dimensions)-spatial-scale transport dynamics indicative of CFTR mobility outside of microdomains. The other population exhibited small-spatial-scale dynamics and displayed confinement consistent with nanoscale membrane domains. Cholesterol depletion reduced CFTR confinement and the fraction of CFTR in the confined population, whereas these were both increased by cholesterol insertion. The results show a clear dependence of CFTR distribution and dynamics on cholesterol and suggest that a fraction of CFTR exists in lipid rafts under physiological conditions. Lipid-raft fusion into large platforms during infection may enhance the regulation of CFTR channel activity or modulate stability of the channel at the cell surface.

MATERIALS AND METHODS

Cell culture and adenovirus infection

Primary human bronchial epithelial (HBE) cells were obtained at first passage from the Cystic Fibrosis Canada Primary Airway Cell Bank at McGill University (see the Supporting Material for details). Cells were seeded on vitrogen-coated (PureCol, Advanced BioMatrix, San Diego, CA), glass-bottom FluoroDishes (World Precision Instruments, Sarasota, FL) and maintained in bronchial epithelial cell growth medium (22) at 37°C. When they reached 80% confluence, they were infected with adenovirus particles directing the expression of green-fluorescent-protein (GFP)-labeled CFTR (GFP-CFTR) (23) at a multiplicity of infection of 100 colony-forming units per cell in OptiMEM medium supplemented with 100 nM vitamin D3 (Calbiochem, Billerica, MA) for 2 days. The cells were rinsed with phosphate-buffered saline and kept in fresh OptiMEM for 2 days, then imaged in OptiMEM with 5% CO_2 at 37°C.

Treatments

All treatments were performed acutely at 37°C. To reduce cholesterol and disrupt lipid rafts, cells were incubated with 1 unit/mL cholesterol oxidase (COase, Sigma, St. Louis, MO) for 30 min before and during imaging. COase was used because in preliminary experiments it was found to cause less cell damage during extended imaging periods compared to methyl-β-cyclodextrin (MβCD). To increase cholesterol production and raft stability, cells were treated with 0.1 unit/mL cholesterol esterase (CEase, Sigma) for 30 min before and during imaging. To examine the acute effects of adenoviral infection on CFTR distribution and dynamics, HBE cells that had already been transduced with GFP-CFTR were exposed to GFP-CFTR adenovirus particles at a multiplicity of infection of 100 for 30 min and then imaged.

Confocal microscopy

Live cell imaging was performed in the Advanced BioImaging Facility of the McGill Life Sciences Complex using an LSM-710 confocal microscope (Zeiss, Jena, Germany), which was equipped with a multiline argon laser (488 nm, 25 mW) and a 561 nm line laser (15 mW). Time-series images were collected from flat regions of the plasma membrane near the coverslip using 0.5% laser power to minimize fluorescence photobleaching. Under these conditions, fluorescence photobleaching was measured to be <10% of the average fluorescence intensity of the first frame of the image series. EGFP was excited using the 488 nm laser line and Alexa-594 was excited at 561 nm. Imaging was performed using a Plan-Apochromat 63× (NA 1.40) oil immersion objective, a confocal pinhole of 1 Airy unit, and a digital gain setting of 900. The experiments were performed on subconfluent, unpolarized HBE cells expressing GFP-CFTR in a humidified cell incubator on the microscope stage maintained at 37°C with 5% CO_2 (Live Cell Instrument, Seoul, South Korea).

The time series consisted of 800 images (256 × 256 pixels) collected from a single cell and focused on an area of membrane in contact with the glass coverslip. Image series were collected at a frame rate of 6.5 Hz, a pixel diameter of 0.06 μm, and a pixel dwell time of 1 μs. For the analysis of confined dynamics, 59–136 image series were analyzed per stimulation condition. For the purpose of visually showing CFTR distribution in the plasma membrane, individual confocal images of a 1024 × 1024 pixel area were collected at 0.2 Hz, with a pixel diameter of 0.13 μm, a dwell time of 6 μs, and laser power of 5% to enhance the signal/noise ratio.

Spatial ICS

ICS was used to measure the degree of aggregation and cluster density for CFTR in cells exposed to different stimuli. The ICS technique has been described in detail elsewhere (19). Briefly, the degree of aggregation (DA) was calculated as

$$DA = \frac{\langle i \rangle}{CD} \tag{1}$$

and the cluster density (CD) as

$$CD = \frac{\langle n_p \rangle}{\pi \omega_0^2}, \tag{2}$$

where CD is the average number of independent fluorescent entities per unit area, $\langle i \rangle$ is the spatial average pixel intensity of the image region of interest (ROI), $\langle n_p \rangle$ is the average number of particles per beam focus, and ω_0 is the e^{-2} beam radius. $\langle n_p \rangle$ is the reciprocal of the zero spatial lags amplitude of the spatial correlation function of the image, which is obtained from a nonlinear least-squares fit of a Gaussian function. Details of the spatial image cross-correlation spectroscopy technique can be found elsewhere (24,25) and in the Supporting Material.

kICS: Theory and analysis

CFTR dynamics were studied using kICS analysis (20,21). Briefly, for this analysis, the k-space time correlation function, $\Phi(\vec{k}; \tau)$, is obtained by calculating the temporal correlation function of the k-space image series

(i.e., after calculating the two-dimensional spatial Fourier transform for each image in the time series) using

$$\Phi(\vec{k};\tau) = \langle \tilde{i}(\vec{k},t)\tilde{i}^*(\vec{k},t+\tau)\rangle, \qquad (3)$$

where $\tilde{i}(\vec{k},t)$ is the Fourier transform of the image acquired at time t, and $\tilde{i}^*(\vec{k},t+\tau)$ is the complex conjugate of the Fourier transform of the image acquired at time $t+\tau$. The angular brackets denote temporal correlation.

For particles undergoing two-dimensional diffusion with a diffusion coefficient D, $\Phi(\vec{k};\tau)$ is analytically written as

$$\Phi(\vec{k};\tau,t) = N\frac{q^2 I_0^2 \omega_0^4 \pi^2}{4} \times \langle \Theta(t)\Theta(t+\tau)\rangle$$
$$\times \exp\left[-|\vec{k}|^2\left(D\tau + \frac{\omega_0^2}{4}\right)\right], \qquad (4)$$

where N is the number of fluorescent particles in the image ROI, q is the quantum yield of the fluorophore, I_0 is the intensity at the center of the beam focus, and ω_0 is the e^{-2} laser-beam radius in the lateral direction at focus. Fluorophore photophysics effects (bleaching and blinking) are accounted for by the time-dependent function, $\Theta(t)$.

The correlation function in Eq. 4 can be simplified to

$$\Phi(\vec{k};\tau,t) = \langle N(t)\rangle \exp\left[-|\vec{k}|^2\left(D\tau + \frac{\omega_0^2}{4}\right)\right], \qquad (5)$$

where $\langle N(t)\rangle$ is proportional to the average number of particles in the ROI and to the time-dependent photophysics effects given in the correlation prefactor amplitude of Eq. 4.

In the case of two different diffusing species (species 1 and 2), the correlation function is the weighted sum of all contributions, computed as

$$\Phi(\vec{k};\tau,t) = \langle N_1\rangle e^{-|\vec{k}|^2\left(D_1\tau+\frac{\omega_0^2}{4}\right)} + \langle N_2\rangle e^{-|\vec{k}|^2\left(D_2\tau+\frac{\omega_0^2}{4}\right)}. \qquad (6)$$

The finite width of the correlation function at the zero temporal lag will mask the motion at spatial scales smaller than the point spread function (PSF). In kICS, the contribution of the finite PSF can be removed by normalizing the correlation function with the zero-temporal-lag correlation function as follows:

$$\frac{\Phi(\vec{k};\tau,t)}{\Phi(\vec{k};0,t)} = \phi_1 e^{-|\vec{k}|^2 D_1\tau} + \phi_2 e^{-|\vec{k}|^2 D_2\tau}, \qquad (7)$$

where ϕ_i is the amplitude of population i in the normalized multicomponent correlation function. It is proportional to N_i and is photophysics- and time dependent:

$$\phi_i = \frac{N_i}{N_i + N_j}\frac{\langle\Theta(t)\Theta(t+\tau)\rangle}{\langle\Theta^2(t)\rangle}. \qquad (8)$$

This two-component model in Eq. 7 can be applied to a system with one particle type that exhibits confined (microscale) and unconfined (macroscale) diffusion dynamics within and between small domains distributed in two dimensions if the exchange occurs on a faster timescale. A fit to this model was used to extract effective diffusion coefficients for the confined (D_{micro}) and unconfined (D_{macro}) particle populations and their respective amplitude parameters.

More specifically, the correlation function is fit to a sum of two Gaussians at each temporal lag τ. The fit parameters are $D_{macro}\tau$, $D_{micro}\tau$, ϕ_{macro}, and ϕ_{micro} as a function of τ. Mean-square displacement (MSD) plots for the

two populations are then constructed from the fit-extracted $D_i\tau$ versus τ, and the amplitude graphs are constructed from the fit-extracted ϕ_i versus τ.

The slope of the macro MSD versus τ plot is D_{macro}, which is an effective diffusion coefficient of CFTR inside and between microdomains (see Fig. S4 in the Supporting Material). For the image sampling rate and membrane CFTR system in this study, the slope of the first three temporal lags of the micro MSD versus τ plot is D_{micro}, which is the diffusion coefficient of particles confined inside the microscopic domains. The fractions that are in the macro and micro populations are then calculated from the amplitudes at long-temporal-lag values τ as $f_{macro} = \phi_{macro}/(\phi_{macro} + \phi_{micro})$ and $f_{micro} = \phi_{micro}/(\phi_{macro} + \phi_{micro})$. According to simulations (20), the recovered D_{macro} and D_{micro} are dependent on the probability of particles escaping from confinement (see the Supporting Material for details). Thus, practically, the D_{macro} describes an apparent diffusion coefficient that includes exchange in addition to simple diffusion outside of domains.

The y-axis intercept of the micro MSD plot extrapolated from long temporal lags τ is $R^2/4$. R is a spatial parameter proportional to the domain radius (d), D_{micro}, and the probability of molecules exiting the domains (P_{out}). Based on simulations, the R-value is $\sqrt{2}\,d$ for domains with radii larger than the PSF radius (20). For domains with radii smaller than the PSF radius, the R-value is twice the pixel diameter. There is a limitation for recovering the actual domain radius due to the background noise of the system and the spatial aliasing which is set by the Nyquist criterion. However, according to simulations, the R-value and domain confinement are inversely related; the smaller the R-value, the stronger the domain confinement, and the larger the R-value, the weaker the confinement (20). This makes the R-value a measure of confinement strength rather than a physical measurement of the domain radius.

For the analysis of CFTR dynamics using kICS, 59–136 image series were analyzed per stimulation condition. The mean of each measured parameter, the standard error, and the t-value were then calculated over n cells (n_{cells}, see Table 1) for statistical significance evaluations.

Statistical analysis

The kICS measured parameters, D_{macro}, D_{micro}, f_{macro}, f_{micro}, and R-value, were presented as the mean $\pm$ SE for n cells. Data sets obtained with different treatments were compared to the control condition using the unpaired Student t-test. Differences with $p < 0.01$ were considered statistically different.

RESULTS

The nature of CFTR clusters on the plasma membrane

Fig. 1 shows a typical confocal image of the plasma membrane of an unpolarized primary HBE cell expressing GFP-CFTR (henceforth called CFTR). Under control conditions (no stimulation), some CFTR was found in bright, PSF-sized fluorescent clusters that were homogeneously distributed

TABLE 1 CFTR confinement parameters using kICS analysis

Treatment	D_{micro} ($\mu m^2/s$)	f_{micro}	R (μm)	n_{cell}
Ctr1	0.009 $\pm$ 0.001	0.27 $\pm$ 0.02	0.293 $\pm$ 0.007	136
+COase	0.014 $\pm$ 0.001[a]	0.20 $\pm$ 0.01[b]	0.324 $\pm$ 0.005[a]	130
+CEase	0.0032 $\pm$ 0.0006[a]	0.38 $\pm$ 0.05[a]	0.224 $\pm$ 0.007[a]	60
Ctr2	0.008 $\pm$ 0.002	0.23 $\pm$ 0.03	0.291 $\pm$ 0.009	55
+Virus	0.0019 $\pm$ 0.0003[a]	0.51 $\pm$ 0.05[a]	0.221 $\pm$ 0.003[a]	59

[a]Significantly different from its respective Ctr, $p < 0.001$.
[b]Significantly different from its respective Ctr, $p < 0.01$.
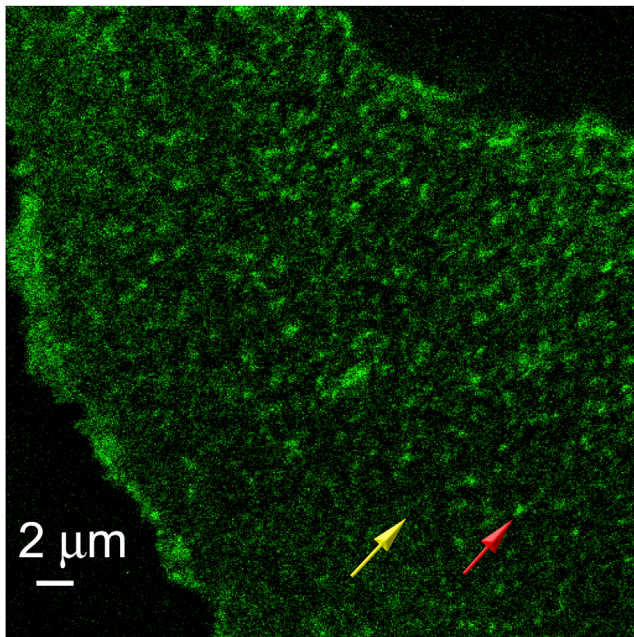
FIGURE 1   CFTR distribution on the plasma membrane of primary HBE cells. A fluorescence confocal microscope image of GFP-CFTR in the plasma membrane of a live HBE cell reveals two populations; one comprised of bright clusters that are homogeneously distributed (*arrow on right*) and another more diffuse population (*arrow on left*). To see this figure in color, go online.

over the plasma membrane (*red arrow*). Diffraction-limited imaging dictates that the actual physical size of the clusters is equal to or smaller than the PSF diameter. CFTR was also visible outside the clusters as diffuse fluorescence (*yellow arrow*) that was significantly more intense than the background autofluorescence, which was negligible under these conditions (Fig. S1). We refer to this diffuse fluorescence as the unconfined CFTR population. The clusters exhibited very slow diffusion (~10^{-4} μm^2/s) and occasional fission events over the course of an image series (123 s). Similar clusters have been described for both glycosylphosphatidylinositol-anchored and epidermal-growth-factor-receptor GFPs, which partition into lipid rafts (26,27).

CFTR clusters were still observed after the cells were sheared off the glass-bottom FluoroDish by sonication so that only the plasma membrane remained attached (Fig. S5; see the Supporting Material for details), suggesting they were in the plasma membrane or closely associated with it in these primary epithelial cells. To rule out the possibility that clusters were sites of clathrin-mediated endocytosis (28), we quantified the colocalization of CFTR clusters with clathrin coated pits using fluorescent transferrin and image cross-correlation spectroscopy analysis (Fig. S6; see the Supporting Material for details). The analysis revealed that only 20% of CFTR clusters were spatially colocalized with clathrin, suggesting that most clusters are unlikely to be undergoing internalization at clathrin-coated pits.

The CFTR aggregation state is cholesterol dependent

In a previous study of Calu-3 airway epithelial cells, CFTR was detected in a DRM fraction after solubilizing airway epithelial cell lysates in ice-cold Tris-buffered saline and fractionating them on a sucrose gradient (4). To test the hypothesis that the clusters in Fig. 1 are CFTR molecules that have aggregated in lipid rafts, we studied the effects of enzyme treatments that are well known to disrupt or enhance lipid rafts in other cell types (29–31). Spatial ICS (19) was used to measure the distribution and aggregation state of CFTR in primary HBE cells (see Materials and Methods for details). COase, an enzyme that converts cholesterol into cholestenone, which does not partition to rafts, was used to disrupt the membrane microdomains (29–33). Reducing cholesterol within these domains would decrease their viscosity and make them weaker traps, which in turn would reduce the amount of CFTR within microdomains and hence its aggregation. Spatial ICS analysis (19) was applied to assess the DA and CD before and after enzyme treatment. After COase treatment, ICS analysis revealed a 30% increase in CFTR CD and a 35% decrease in DA (Fig. 2). These results indicate that stability, cell surface density, and size of CFTR clusters are cholesterol dependent, consistent with their association with membrane microdomains.

To further establish that CFTR clusters are associated with rafts, HBE cells were exposed to CEase, which catalyzes the synthesis of cholesterol and increases its concentration in the plasma membrane. ICS analysis revealed a twofold decrease in CD and a threefold increase in DA after CEase treatment (Fig. 2). The increase in DA and decrease
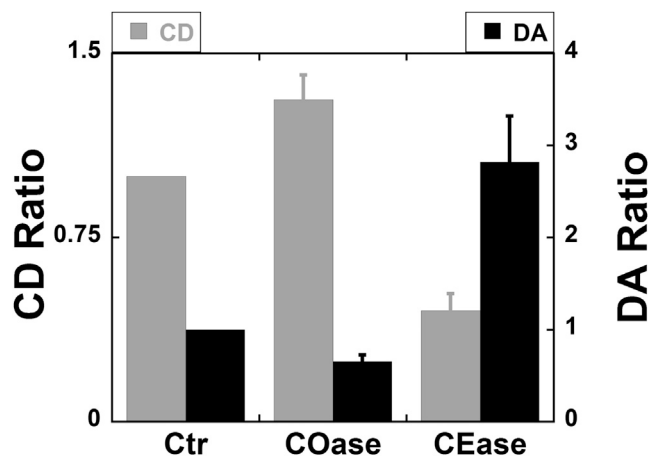

FIGURE 2   CFTR CD and DA in the plasma membrane as measured by spatial ICS are strongly cholesterol dependent. CD and DA were normalized to their control values, the CD ratio and the DA ratio, respectively. In the COase condition, cholesterol loss increased the CFTR CD by 30% and decreased the DA by 35% ($p < 0.01$). Elevating cholesterol in the membrane using CEase reduced the CD by twofold and increased the DA by threefold ($p < 0.01$). Error bars indicate the mean $\pm$ SE.

in CD when cholesterol is augmented may reflect increased fusion of adjacent rafts into large confinement zones in the membrane. Regardless, the effects of manipulating cholesterol on the CFTR aggregation state strongly suggest that a population of CFTR resides within lipid rafts.

CFTR confinement is cholesterol dependent

Confocal-laser-scanning-microscopy imaging under the different treatments shown in Fig. 3, *a–c*, highlights the dependence of CFTR clustering on cholesterol. Conditions that cause cholesterol loss from the membrane reduced the density and brightness of the clusters (Fig. 3 *b*, +*COase*) whereas those that elevate cholesterol increased cluster size and brightness (Fig. 3 *c*, +*CEase*) relative to control conditions (Fig. 3 *a*). These results link the stability and loss of CFTR clusters with the formation and disruption of lipid rafts, and they strongly suggest that CFTR clusters are associated with cholesterol-rich microdomains.

To explore this further, we investigated CFTR dynamics and confinement in the plasma membrane using an extension of the kICS technique (20,21). This analysis uses a confocal image series of GFP-CFTR to calculate the k-space time correlation function for an ROI, as shown in Fig. S2 *a*.
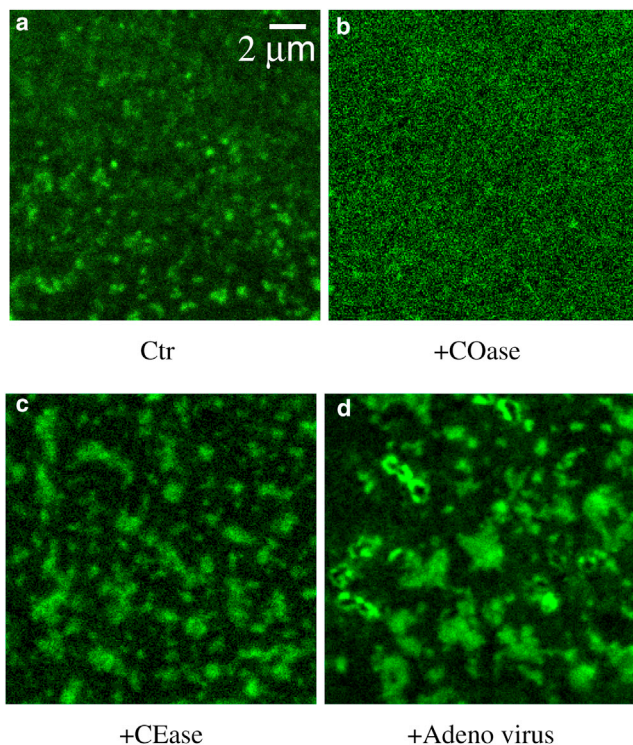

FIGURE 3   CFTR distribution in the plasma membrane depends on membrane cholesterol. (*a*) A confocal microscope image of GFP-CFTR in an ROI on the plasma membrane of live HBE cells under Ctr conditions. (*b*) After lipid raft disruption (+COase). (*c*) After membrane cholesterol insertion (+CEase). (*d*) After acute viral infection (+adenovirus). To see this figure in color, go online.
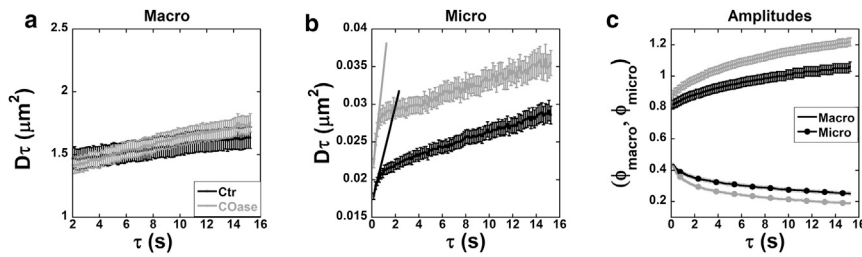
The k-space time correlation function is fitted with a two-component model that accounts for confined diffusion within a microscopic domain and macroscopic effective diffusion of CFTR (i.e., the micro and macro components, respectively). We infer that bright clusters on the plasma membrane of cells expressing GFP-CFTR (Fig. 1) represent CFTR molecules that have partitioned into lipid rafts and that display confined mobility that can be measured using kICS as D_{micro}. The diffuse background fluorescence, on the other hand, is considered to represent the CFTR population that is outside rafts and has a macroscopic diffusion coefficient proportional to D_{macro} (see Fig. S4). The distributions of these two distinct CFTR populations detected by kICS have fit amplitudes ϕ_{micro} and ϕ_{macro}, which are normalized to obtain the fraction of CFTR in each population, f_{micro} and f_{macro} (see Materials and Methods). kICS was used to study the effects of cholesterol reduction (+COase) and insertion (+CEase) on the macroscopic- and microscopic-scale dynamics of these CFTR populations and their respective fractions in the membrane.

Cholesterol depletion reduces CFTR confinement

MSD plots calculated for unconfined and confined populations of CFTR ($D_{macro}\tau$ and $D_{micro}\tau$ versus τ) and the lag-time-dependent amplitude plots ($\phi_{macro}(\tau)$ and $\phi_{micro}(\tau)$ versus τ) under control (Ctr) conditions and after COase are shown in Fig. 4. The MSD plot for the unconfined population (Fig. 4 *a*) has a steeper slope after COase treatment, indicating an increase in D_{macro} (Ctr, $D_{macro} = 0.014 \pm 0.003$ μm^2/s; COase, $D_{macro} = 0.026 \pm 0.002$ μm^2/s). Dynamics of the confined CFTR population also increased after COase treatment, as evidenced by the steeper initial slope of the MSD curve for the micro component (the linear fit of the first three temporal lags: Ctr, $D_{micro} = 0.009 \pm 0.001$ μm^2/s, COase: $D_{micro} = 0.014 \pm 0.001$ μm^2/s) (Fig. 4 *b*). The increase in D_{micro} indicates an increase in CFTR exchange dynamics into and out of lipid rafts after enzyme exposure. This would be explained if reducing raft cholesterol reduced their viscosity, making them weaker traps for CFTR. The amplitude of the confined CFTR population (ϕ_{micro}) declined significantly after raft disruption by COase, whereas that of the unconfined population (ϕ_{macro}) was increased (Fig. 4 *c*), demonstrating a redistribution of CFTR between the two populations. A summary of the fit parameters D_{macro}, D_{micro}, f_{macro}, and f_{micro} for each cell population during Ctr and COase treatment is shown in Fig. 5 and Table 1. Fig. 5 shows that ~25% of CFTR in the plasma membrane was in the confined population under the control conditions, and this fraction was reduced when rafts were disrupted by COase.

Cholesterol insertion stabilizes CFTR within lipid rafts

Cholesterol promotes the formation of microdomains and increases their viscosity (32,33). If a population of CFTR channels partitions into rafts, augmenting cholesterol in

FIGURE 4 CFTR macro- and microdynamics and distribution on the plasma membrane are cholesterol dependent. (*a*) The average macroscale MSD, $D_{macro}\tau$, increased linearly as a function of τ for control (*Ctr, black*) and COase-treated cells (*gray*). The slope, D_{macro}, is the macro diffusion coefficient of unconfined CFTR. (*b*) The average microscale MSD, $D_{micro}\tau$, increased linearly for the first few temporal lags and dramatically changed its slope at a later τ for both conditions. The first three temporal lags were fit with straight lines, as shown, yielding a slope, D_{micro}, that describes the mobility of the CFTR population inside confinements. COase treatment resulted in a larger D_{micro} compared to the Ctr condition, indicating a weaker trap. (*c*) The average amplitudes of the macro- (ϕ_{macro}, *line*) and microcomponents (ϕ_{micro}, *solid circles*) of the k-space correlation function as a function of τ. For n_{cell} averages, see Table 1. Error bars indicate the mean $\pm$ SE.

the raft with CEase should increase the efficiency of CFTR confinement. Fig. 5 *a* shows that diffusion coefficients for the unconfined (D_{macro}) and confined (D_{micro}) populations of CFTR were both reduced by CEase treatment. Moreover, the fraction of CFTR in the unconfined population (f_{macro}) declined, whereas the confined fraction (f_{micro}) was significantly increased (Fig. 5 *b*). The confinement parameters obtained for Ctr and CEase treatment using kICS analysis are shown in Table 1. This strongly supports the hypothesis that two populations of CFTR molecules exist in the plasma membrane, one of which is localized to lipid rafts.

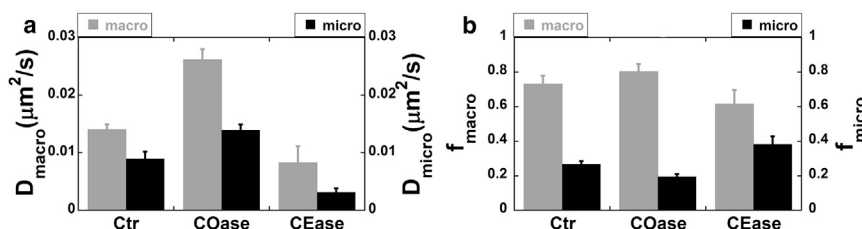## CFTR confinement strength is cholesterol dependent

The *y*-intercept of the micro MSD-versus-τ plot extrapolated from long temporal lags yields the *R*-value, which is a measure of confinement strength within lipid microdomains (see Materials and Methods for details). Simulations indicate an inverse relationship between R and confinement strength: the larger the *R*-value, the weaker the traps, and vice versa (20). It can be seen in Fig. S7 *a* that cholesterol depletion from the membrane (i.e., COase treatment) significantly increased the *R*-value, consistent with a decrease in CFTR confinement. Conversely, cholesterol insertion into the membrane (+CEase) dramatically decreased the *R*-value, indicating increased confinement in rafts (see Table 1). Taken together, these results indicate that membrane cholesterol is a determinant of CFTR populations through its effects on confinement. Cholesterol depletion reduces CFTR confinement strength by allowing proteins to escape

from membrane rafts, whereas cholesterol insertion increases it, probably through an increase in raft viscosity.

CFTR confinement increases when large platforms form in response to acute viral infection

Bacteria and viruses trigger the hydrolysis of sphingomyelin in lipid rafts to ceramide, which leads to the aggregation of the rafts into large membrane platforms (34–36). Exposure to pathogens leads to ceramide synthesis and the formation of large platforms that are essential for their entry into airway epithelial cells (14,16,34,35,37). We studied the effects of acute adenoviral infection on the transformation of nanoscale lipid rafts into large platforms and on the distribution and dynamics of CFTR using kICS.

Within minutes of exposure to adenovirus particles, punctate clusters of CFTR began to coalesce into 1- to 2-μm-diameter platforms (see Fig. 3 *d*). This was accompanied by striking decreases in D_{macro} and D_{micro} (Fig. 6 *a*) and a redistribution between the two CFTR populations (Fig. 6 *b*). The fraction displaying macroscopic dynamics (f_{macro}) decreased, whereas the confined population (f_{micro}) increased dramatically (Fig. 6 *b*). Viral infection also caused a dramatic reduction in the *R*-value (Fig. S7 *b*), confirming that recruitment into large ceramide platforms dramatically increased CFTR confinement. Table 1 summarizes the effects of acute viral infection on the confinement parameters. In summary, viral infection induces the fusion of CFTR-containing rafts into large platforms where CFTR mobility is greatly reduced, and it also leads to recruitment of CFTR from the unconfined population.

FIGURE 5 CFTR macro- and microdynamics and distribution on the plasma membrane are cholesterol dependent. (*a*) Both D_{macro} and D_{micro} of CFTR increased significantly after cholesterol depletion from the membrane (+*COase*) and decreased significantly after cholesterol augmentation (+*CEase*). (*b*) Gray bars indicate the unconfined population fraction, f_{macro}, increased by cholesterol loss (+*COase*) and decreased after cholesterol insertion (+*CEase*). Black bars indicate the confined population fraction of CFTR, f_{micro}, decreased significantly after COase and increased significantly after CEase. Error bars indicate the mean $\pm$ SE.
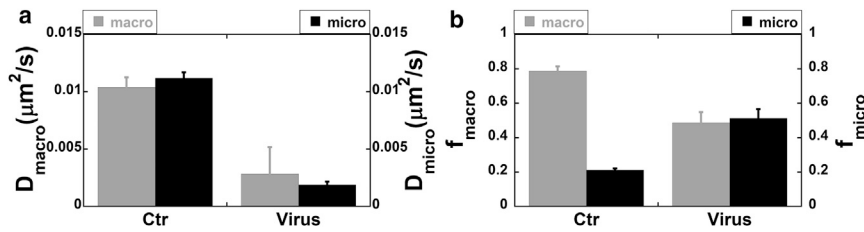
FIGURE 6 CFTR dynamics and distribution after acute viral infection. (*a*) Both the D_{macro} and D_{micro} of CFTR decreased significantly after the infection. (*b*) Although the unconfined population fraction, f_{macro}, decreased significantly postinfection (*gray*), the confined population fraction, f_{micro}, increased by twofold (*black*). This indicates recruitment of CFTR to confinement zones during infection. Error bars indicate the mean $\pm$ SE.

DISCUSSION

This study distinguishes two CFTR populations on the plasma membrane of primary HBE cells, one that is in clusters and another that is diffusely distributed. Quantitative analyses of image time series also revealed two populations of CFTR molecules based on lateral mobility in the membrane. One displayed confinement and slow dynamics and was sensitive to membrane cholesterol concentration. The other was more abundant, relatively unconfined, and more rapidly diffusing. The existence of two populations is consistent with biochemical data showing that ~50% of the total CFTR in the airway epithelial cell line Calu-3 occurs in a cholesterol-rich DRM fraction (4,8). Therefore, a straightforward interpretation of the imaging data is that some CFTR molecules at the cell surface reside in nanoscale cholesterol- and sphingolipid-rich microdomains (lipid rafts). We quantified the distribution of CFTR between microdomains and bulk membrane on live cells and studied CFTR dynamics within each population. Finally, we examined the effects of acute viral infection quantitatively and found aggregation of preexisting CFTR clusters into large platforms similar to those described previously during infection by *Pseudomonas aeruginosa* (34) and rhinoviruses (35).

The cell model

First-passage primary HBEs differentiate into a pseudostratified layer that is remarkably similar to airway surface epithelium in vivo when they are cultured at the air-liquid interface. The quantitative imaging methods used here required an area of flat membrane, so we used unpolarized cells and imaged GFP-CFTR in the plasma membrane that was in contact with the collagen-covered glass coverslip. This enabled the analysis of CFTR dynamics but also allowed mixing of apical and basolateral membrane constituents. It is not known whether identical CFTR dynamics would be observed in pure apical membrane, but platforms very similar to those induced by adenovirus in this study have been reported after infection of fully polarized cells in vivo (34). It is also worth noting that epithelial cell polarity is transiently lost in vivo, for example, during injury by the gram-positive bacterium *Staphylococcus aureus*, which usually infects CF airways before *Pseudomonas aeruginosa*. Wild-type GFP-CFTR was expressed in cells isolated from patients that were homozygous for the F508del muta-

tion, which ensured that the plasma membrane contained little, if any, endogenous nonfluorescent CFTR. A replication-deficient adenoviral vector lacking most of the viral genome was used for efficient GFP-CFTR expression. Capsid proteins on the adenovirus particles can trigger interferon and inflammatory responses in HBEs, and acute exposure did cause CFTR clusters to coalesce into large platforms. However, the innate immune response to adenovirus subsides within 1–2 days in most cell types, and the absence of platforms under control conditions 4 days posttransduction suggests that adenoviral delivery of GFP-CFTR did not have a persistent effect on CFTR dynamics.

CFTR clustering is cholesterol dependent

GFP-CFTR clusters remained after the cells had been sheared from the coverslip, indicating that they are intimately associated with the plasma membrane (Figs. 1 and S5). This punctate distribution of GFP-CFTR was also observed in the immortalized CF cell line CFBE after adenoviral transduction or plasmid electroporation. Importantly, it was affected by changes in membrane cholesterol that affect the properties and composition of lipid rafts. Although the precise nature of the aggregates remains uncertain, only 20% were colocalized with fluorescent transferrin; therefore, most CFTR clusters were not situated in clathrin-coated pits that mediate CFTR internalization. To explore the possibility that CFTR clusters reflect confinement in cholesterol-rich lipid rafts, we used enzymes that are known to alter the amount of cholesterol in the membrane. Cholesterol depletion by COase reduced the number and brightness of CFTR clusters compared to untreated control cells (Fig. 3 *b*) and reduced the degree of aggregation (Fig. 2), suggesting that the formation and stability of clusters are cholesterol dependent. Conversely, augmenting membrane cholesterol using CEase increased the average size of the clusters (Fig. 3 *c*) and the degree of aggregation (Fig. 2), consistent with cholesterol promoting the formation of lipid rafts or their fusion into larger domains that sequester CFTR.

Comparison of kICS and single-particle tracking for studies of CFTR confinement

Single-particle tracking (SPT) (38) has been used to examine CFTR dynamics at the cell surface (18,39). In

the first study, quantum-dot labeling after specific biotinylation of wild-type CFTR revealed very low mobility (average microscale diffusion coefficient, ~5 × 10⁻³ μm^2/s (39)). Wild-type CFTR was predominantly tethered, whereas mobility was dramatically increased in a mutant that had 10 histidine residues added to the C-terminus to inhibit binding by NHERF and other PDZ-domain proteins. The 10-His mutant displayed transient confinement suggestive of residual protein-protein interactions. Near immobilization of wild-type CFTR was confirmed using CFTR that was labeled with antibody-coated quantum dots, although transient confinement was not detected when NHERF binding was disrupted (18). Finally, a study with antibodies conjugated to colloidal gold revealed transient confinement of wild-type CFTR, which was reduced by mutation of a filamin binding site near the amino terminus (40). None of these studies reported an association of CFTR with lipid rafts.

SPT yields precise information regarding molecular trajectories but requires dilute (usually exofacial) labeling with bright fluorophores so that single molecules can be resolved (41). The kICS analysis used here is more suited for studying populations because it is an ensemble method that can be applied to fluorescently-tagged proteins anywhere in the cell and over a wide range of expression levels (42). Ensemble averaging of kICS data allows separate analysis of the micro- and macroscale dynamics and the resulting D_{macro}, D_{micro}, and domain radii are limited only by the background noise and the spatial and temporal resolution of the image time series. Multicomponent fitting of the kICS correlation function provides average results for large numbers of cells, facilitating statistical comparisons over very different time- and lengthscales. The kICS analysis described here provides the first evidence, to our knowledge, that cholesterol influences CFTR mobility and confinement. Our estimate of the microscale diffusion coefficient 6–10 × 10⁻³ μm^2/s is well within the range of confined dynamics reported previously; thus, CFTR partitioning in the plasma membrane likely involves interactions with both cytoskeletal elements and lipid rafts.

CFTR confinement and dynamics are influenced by cholesterol

Approximately 25% of the CFTR in the plasma membrane of primary HBE cells was confined under unstimulated (control) conditions, consistent with localization in lipid rafts. The confined population was reduced by 20% after cells were exposed to COase, but it was not eliminated. COase is a relatively mild treatment and is expected to cause only partial depletion of membrane cholesterol, so 20% is likely an underestimate of the fraction confined to membrane microdomains. More complete extraction of cholesterol would be expected with MβCD, but preliminary experiments have revealed that MβCD causes cell damage during long-term imaging experiments. The modest decrease in confined CFTR molecules may reflect the fraction that is in cholesterol-

sphingomyelin rafts, with the other 80% being confined by ceramide-based rafts or attachments to the actin cytoskeleton. Elevating cholesterol with cholesterol esterase caused the fraction of CFTR displaying confinement to double. Since cholesterol is a major component of lipid rafts, promoting its insertion into the plasma membrane may increase lipid raft density and/or viscosity. Taken together, the opposing effects of depleting and elevating cholesterol levels provide further evidence for CFTR partitioning into cholesterol-rich membrane microdomains.

Fluorescence-recovery-after-photobleaching studies indicate that 40–50% of the CFTR on IB3-1 and BHK cells has very slow dynamics and does not recover in the photobleached region (15,39). Similar results were obtained using temporal image correlation spectroscopy analysis (39). The contribution of cholesterol-rich microdomains to CFTR dynamics was not examined, but more recent studies have detected 6–48% of the total CFTR from Calu-3 cells in a DRM fraction (4,8).

The results presented here indicate that the lateral mobility of a CFTR population is cholesterol dependent, consistent with confinement in cholesterol-rich microdomains (lipid rafts). Cholesterol depletion significantly increased D_{micro}, suggesting that they were weaker traps. D_{macro} increased as well since large spatial scale dynamics are also influenced by transient confinements. Reduced trapping was also evident as an increase in the R-value, indicating a decrease in the confinement strength. On the other hand, enhancing cholesterol insertion with CEase dramatically reduced D_{micro}, probably through enhanced sphingomyelin packing, which increased order within the microdomains. Trapping was expected to reduce D_{micro}, D_{macro}, and the R-value, and this was observed. To our knowledge, these results present the first biophysical quantification of CFTR partitioning into cholesterol-rich microdomains in the plasma membrane of live cells.

kICS analysis together with the spatial ICS analysis showed that elevating membrane cholesterol reduces the CFTR CD by twofold, increases the DA by threefold, dramatically increases the fraction of CFTR molecules displaying microscale dynamics, f_{micro}, increases CFTR confinement strength (i.e., R-value), and reduces small-spatial-scale dynamics, D_{micro}. The decline in CFTR CD suggests a decrease in the density of lipid rafts after cholesterol insertion, perhaps due to formation of larger lipid rafts or the fusion of microdomains as shown in Fig. 3 c. The increase in DA and f_{micro} and the decrease in D_{micro} suggest that lipid raft viscosity and CFTR confinement are increased after cholesterol insertion, probably due to enhanced sphingomyelin packing.

CFTR platforms after viral infection

CFTR is central to innate immunity in the airways through its roles in mucociliary clearance, bicarbonate-dependent bacterial killing, and perhaps direct binding and internalization of bacteria (14–16,37,43). Exposing airway epithelial

cells to *Pseudomonas aeruginosa* causes lipid rafts to fuse into large ceramide-rich platforms, which leads to internalization of the bacterium, apoptosis and cytokine release (34). Infection by some viruses is also enhanced by the hydrolysis of membrane sphingomyelin to ceramide (35,36). We found that acute exposure to adenovirus particles had rapid effects on CFTR mobility. Within 30 min, CFTR dynamics decreased >80% with a pronounced shift of unconfined CFTR to the confined population, consistent with fusion of nanoscale lipid rafts containing CFTR clusters into much larger platforms 1–2 μm in diameter (Fig. 3 *d*). These acute effects resemble those described previously during *Pseudomonas aeruginosa* infection (34). The platforms were transient; they were not observed 4 days postinfection under control conditions, further evidence that cells had recovered from any interferon or inflammatory responses to the adenoviral vector delivery of CFTR.

CONCLUSIONS

To our knowledge, these studies provide the first biophysical evidence that CFTR exists in two populations at the cell surface, one of which is influenced by cholesterol. Since cholesterol is an important constituent of lipid rafts, this strongly suggests that one of the CFTR populations is situated in lipid rafts under unstimulated conditions. Clustering and confinement in lipid rafts may modulate CFTR channel function as the membrane microdomains are known to recruit kinases and other signaling molecules that regulate CFTR. NHERF1, a scaffold protein that tethers CFTR to the actin cytoskeleton and stabilizes it in the plasma membrane, is especially interesting in this regard as it has a cholesterol binding motif (13). Whether this motif helps target NHERF1 and its interactome to rafts remains to be determined. The incorporation of CFTR into large ceramide-rich platforms through the fusion of lipid rafts may be a mechanism by which CFTR expression and channel function are elevated at the cell surface.

SUPPORTING MATERIAL

Supporting Materials and Methods, Supporting Results, seven figures, and one table are available at http://www.biophysj.org/biophysj/supplemental/S0006-3495(15)00550-0.

AUTHOR CONTRIBUTIONS

A.A.A. designed and performed research, provided analysis codes, analyzed data, and wrote the article. E.P. provided analysis codes and analyzed data. J.G. and E.M. provided primary HBE cells. J.W.H. and P.W.W. designed the research and wrote the article.

ACKNOWLEDGMENTS

SUPPORTING CITATIONS

References (44–47) appear in the Supporting Material.

REFERENCES

1. Guggino, W. B., and B. A. Stanton. 2006. New insights into cystic fibrosis: molecular switches that regulate CFTR. *Nat. Rev. Mol. Cell Biol.* 7:426–436.

2. Penmatsa, H., W. Zhang, …, A. P. Naren. 2010. Compartmentalized cyclic adenosine 3′,5′-monophosphate at the plasma membrane clusters PDE3A and cystic fibrosis transmembrane conductance regulator into microdomains. *Mol. Biol. Cell.* 21:1097–1110.

3. Frizzell, R. A., and J. W. Hanrahan. 2012. Physiology of epithelial chloride and fluid secretion. *Cold Spring Harb. Perspect. Med.* 2:a009563.

4. Wang, D., W. Wang, …, P. Huang. 2008. Functional coupling of Gs and CFTR is independent of their association with lipid rafts in epithelial cells. *Pflugers Arch.* 456:929–938.

5. Calder, P. C., and P. Yaqoob. 2007. Lipid rafts—composition, characterization, and controversies. *J. Nutr.* 137:545–547.

6. Simons, K., and D. Toomre. 2000. Lipid rafts and signal transduction. *Nat. Rev. Mol. Cell Biol.* 1:31–39.

7. Patel, H. H., F. Murray, and P. A. Insel. 2008. G-protein-coupled receptor-signalling components in membrane raft and caveolae microdomains. *Handb. Exp. Pharmacol.* 2008:167–184.

8. Dudez, T., F. Borot, …, M. Chanson. 2008. CFTR in a lipid raft-TNFR1 complex modulates gap junctional intercellular communication and IL-8 secretion. *Biochim. Biophys. Acta.* 1783:779–788.

9. Arcaro, A., M. Aubert, …, M. J. Seckl. 2007. Critical role for lipid raft-associated Src kinases in activation of PI3K-Akt signalling. *Cell. Signal.* 19:1081–1092.

10. Bi, K., Y. Tanaka, …, A. Altman. 2001. Antigen-induced translocation of PKC-θ to membrane rafts is required for T cell activation. *Nat. Immunol.* 2:556–563.

11. Steinberg, S. F. 2008. Structural basis of protein kinase C isoform function. *Physiol. Rev.* 88:1341–1378.

12. Short, D. B., K. W. Trotter, …, S. L. Milgram. 1998. An apical PDZ protein anchors the cystic fibrosis transmembrane conductance regulator to the cytoskeleton. *J. Biol. Chem.* 273:19797–19801.

13. Sheng, R., Y. Chen, …, W. Cho. 2012. Cholesterol modulates cell signaling and protein networking by specifically interacting with PDZ domain-containing scaffold proteins. *Nat. Commun.* 3:1249.

14. Kowalski, M. P., and G. B. Pier. 2004. Localization of cystic fibrosis transmembrane conductance regulator to lipid rafts of epithelial cells is required for *Pseudomonas aeruginosa*-induced cellular activation. *J. Immunol.* 172:418–425.

15. Bajmoczi, M., M. Gadjeva, ..., D. E. Golan. 2009. Cystic fibrosis trans-membrane conductance regulator and caveolin-1 regulate epithelial cell internalization of *Pseudomonas aeruginosa*. *Am. J. Physiol. Cell Physiol.* 297:C263–C277.

16. Zaidi, T., M. Bajmoczi, ..., G. B. Pier. 2008. Disruption of CFTR-dependent lipid rafts reduces bacterial levels and corneal disease in a murine model of *Pseudomonas aeruginosa* keratitis. *Invest. Ophthalmol. Vis. Sci.* 49:1000–1009.

17. Vij, N., S. Mazur, and P. L. Zeitlin. 2009. CFTR is a negative regulator of NFkappaB mediated innate immune response. *PLoS ONE.* 4:e4664.

18. Haggie, P. M., J. K. Kim, ..., A. S. Verkman. 2006. Tracking of quantum dot-labeled CFTR shows near immobilization by C-terminal PDZ interactions. *Mol. Biol. Cell.* 17:4937–4945.

19. Wiseman, P. W., and N. O. Petersen. 1999. Image correlation spectroscopy. II. Optimization for ultrasensitive detection of preexisting platelet-derived growth factor-β receptor oligomers on intact cells. *Biophys. J.* 76:963–977.

20. Pandzic, E. 2013. Confinement in image correlation spectoscopy. PhD thesis. McGill University, Montreal, Canada.

21. Kolin, D. L., D. Ronis, and P. W. Wiseman. 2006. k-Space image correlation spectroscopy: a method for accurate transport measurements independent of fluorophore photophysics. *Biophys. J.* 91:3061–3075.

22. Fulcher, M. L., S. Gabriel, ..., S. H. Randell. 2005. Well-differentiated human airway epithelial cell cultures. *Methods Mol. Med.* 107: 183–206.

23. Vais, H., G. P. Gao, ..., W. W. Reenstra. 2004. Novel adenoviral vectors coding for GFP-tagged wtCFTR and deltaF508-CFTR: characterization of expression and electrophysiological properties in A549 cells. *Pflugers Arch.* 449:278–287.

24. Wiseman, P. W., J. A. Squier, ..., K. R. Wilson. 2000. Two-photon image correlation spectroscopy and image cross-correlation spectroscopy. *J. Microsc.* 200:14–25.

25. Comeau, J. W. D., S. Costantino, and P. W. Wiseman. 2006. A guide to accurate fluorescence microscopy colocalization measurements. *Biophys. J.* 91:4611–4622.

26. Nohe, A., E. Keating, ..., N. O. Petersen. 2006. Dynamics of GPI-anchored proteins on the surface of living cells. *Nanomedicine (Lond. Print).* 2:1–7.

27. Keating, E., A. Nohe, and N. O. Petersen. 2008. Studies of distribution, location and dynamic properties of EGFR on the cell surface measured by image correlation spectroscopy. *Eur. Biophys. J.* 37:469–481.

28. Bradbury, N. A., J. A. Clark, ..., R. J. Bridges. 1999. Characterization of the internalization pathways for the cystic fibrosis transmembrane conductance regulator. *Am. J. Physiol.* 276:L659–L668.

29. Lenne, P. F., L. Wawrezinieck, ..., D. Marguet. 2006. Dynamic molecular confinement in the plasma membrane by microdomains and the cytoskeleton meshwork. *EMBO J.* 25:3245–3256.

30. von Tresckow, B., K. J. Kallen, ..., H. P. Hansen. 2004. Depletion of cellular cholesterol and lipid rafts increases shedding of CD30. *J. Immunol.* 172:4324–4331.

31. Samsonov, A. V., I. Mihalyov, and F. S. Cohen. 2001. Characterization of cholesterol-sphingomyelin domains and their dynamics in bilayer membranes. *Biophys. J.* 81:1486–1500.

32. Nipper, M. E., S. Majd, ..., M. A. Haidekker. 2008. Characterization of changes in the viscosity of lipid membranes with the molecular rotor FCVJ. *Biochim. Biophys. Acta.* 1778:1148–1153.

33. Pralle, A., P. Keller, ..., J. K. H. Hörber. 2000. Sphingolipid-cholesterol rafts diffuse as small entities in the plasma membrane of mammalian cells. *J. Cell Biol.* 148:997–1008.

34. Grassmé, H., V. Jendrossek, ..., E. Gulbins. 2003. Host defense against *Pseudomonas aeruginosa* requires ceramide-rich membrane rafts. *Nat. Med.* 9:322–330.

35. Grassmé, H., A. Riehle, ..., E. Gulbins. 2005. Rhinoviruses infect human epithelial cells via ceramide-enriched membrane platforms. *J. Biol. Chem.* 280:26256–26262.

36. Tani, H., M. Shiokawa, ..., Y. Matsuura. 2010. Involvement of ceramide in the propagation of Japanese encephalitis virus. *J. Virol.* 84:2798–2807.

37. Colasurdo, G. N., J. J. Fullmer, ..., J. M. Stark. 2006. Respiratory syncytial virus infection in a murine model of cystic fibrosis. *J. Med. Virol.* 78:651–658.

38. Saxton, M. J., and K. Jacobson. 1997. Single-particle tracking: applications to membrane dynamics. *Annu. Rev. Biophys. Biomol. Struct.* 26:373–399.

39. Bates, I. R., B. Hébert, ..., J. W. Hanrahan. 2006. Membrane lateral diffusion and capture of CFTR within transient confinement zones. *Biophys. J.* 91:1046–1058.

40. Thelin, W. R., Y. Chen, ..., S. L. Milgram. 2007. Direct interaction with filamins modulates the stability and plasma membrane expression of CFTR. *J. Clin. Invest.* 117:364–374.

41. Clausen, M. P., E. C. Arnspang, ..., B. C. Lagerholm. 2014. Simultaneous multi-species tracking in live cells with quantum dot conjugates. *PLoS ONE.* 9:e97671.

42. Arnspang, E. C., J. Schwartzentruber, ..., B. C. Lagerholm. 2013. Bridging the gap between single molecule and ensemble methods for measuring lateral dynamics in the plasma membrane. *PLoS ONE.* 8:e78096.

43. Pezzulo, A. A., X. X. Tang, ..., J. Zabner. 2012. Reduced airway surface pH impairs bacterial killing in the porcine cystic fibrosis lung. *Nature.* 487:109–113.

44. Randell, S. H., L. Walstad, ..., J. R. Yankaskas. 2001. Isolation and culture of airway epithelial cells from chronically infected human lungs. *In Vitro Cell. Dev. Biol. Anim.* 37:480–489.

45. Avery, J., D. J. Ellis, ..., R. Jahn. 2000. A cell-free system for regulated exocytosis in PC12 cells. *J. Cell Biol.* 148:317–324.

46. Santini, F., and J. H. Keen. 1996. Endocytosis of activated receptors and clathrin-coated pit formation: deciphering the chicken or egg relationship. *J. Cell Biol.* 132:1025–1036.

47. Prigozhina, N. L., and C. M. Waterman-Storer. 2006. Decreased polarity and increased random motility in PtK1 epithelial cells correlate with inhibition of endosomal recycling. *J. Cell Sci.* 119:3571–3582.